A Journal of the Gesellschaft Deutscher Chemiker

Angewandte International Edition GDCh Chemie

www.angewandte.org

Accepted Article

Title: Unlocking the Power of Lewis Basicity in Oxide Lattice Oxygens: A Regulating Force for Enhanced Oxygen Evolution Kinetics in Li-O2 Batteries

Authors: Hao-Min Guan, Zhi-Peng Cai, Xue-Yan Wu, Kai-Xue Wang, and Jie-Sheng Chen

To be cited as: *Angew. Chem. Int. Ed.* **2025**, e202509132

Link to VoR: https://doi.org/10.1002/anie.202509132

WILEY VCH

10.1002/anie.202509132

WILEY VCH

RESEARCH ARTICLE

Unlocking the Power of Lewis Basicity in Oxide Lattice Oxygens: A Regulating Force for Enhanced Oxygen Evolution Kinetics in Li-O_2 Batteries

Hao-Min Guan,[a, b] Zhi-Peng Cai,[a] Xue-Yan Wu,[c] Kai-Xue Wang*[a] and Jie-Sheng Chen*[a]

[a] H. Guan, Z. Cai, Prof. K. Wang, Prof. J. Chen
School of Chemistry and Chemical Engineering
Shanghai Jiao Tong University
Shanghai 200240 (P. R. China)
E-mail: k.wang@sjtu.edu.cn (Prof. K. Wang); chemcj@sjtu.edu.cn (Prof. J. Chen)

[b] H. Guan, Prof. K. Wang, Prof. J. Chen
Zhiyuan College
Shanghai Jiao Tong University
Shanghai 200240 (P. R. China)

[c] Prof. X. Wu
School of Materials Science and Engineering
Shanghai Jiao Tong University
Shanghai 200240 (P. R. China)

Supporting information for this article is given via a link at the end of the document.

Abstract: Lithium-oxygen batteries (LOBs) require fast oxygen conversion kinetics to achieve good cycling performance and high energy efficiency. In the text of catalysts for LOBs, Lewis basicity of lattice oxygens (O_L) in common transition metal oxides is often underestimated due to the weak electron donor characteristic of O_L. In this work, a new spinel-type high entropy oxide with Lewis basicity (LB-HEO) was synthesized through a Joule-heating method. O_L was activated by regulating the tetrahedral site-O_L-octahedral site (M_{Td}-O_L-M_{Oh}) units in the spinel-type HEO, enhancing the Lewis basicity. Used as cathode catalyst for LOBs, LB-HEO could attract Li^+ and increase the disorder in discharge product, lithium peroxide (Li_2O_2), promoting the delithiation process and the interfacial charge transfer at the LB-HEO|Li_2O_2 interface. The activation energy of interfacial charge transfer was significantly reduced from 63.5 kJ mol^{-1} to 22.4 kJ mol^{-1}. As a result, low charging overpotential of 0.97 V and long cycling lifespan of 135 cycles at 100 mA g^{-1} were achieved with capacity limitation of 1000 mAh g^{-1}. The strategy based on the regulation of Li^+ behavior through its interaction with Lewis bases provides a promising prospective for the design of non-noble metal catalysts for high-performance LOBs.

Introduction

Rechargeable nonaqueous lithium-oxygen batteries (LOBs) with energy density exceeding 3500 Wh kg^{-1} show great potential in energy storage.[1-4] However, the electrode reaction of LOBs involves the complicated transformation among gaseous O_2, soluble LiO_2 and solid Li_2O_2, leading to insufficient interfacial charge transfer kinetics and sluggish oxygen evolution reaction (OER) kinetics during the charging process. As a result, the general charging potential of LOBs is about 1.5 V higher than the theoretical value (2.96 V vs. Li/Li^+) and the energy efficiency of LOBs is low. Oxygen species (O_2, O_2^-, and O_2^{2-}) involved in the discharge/charge processes of LOBs could be considered as Lewis bases, which are more likely to be attracted by Lewis acids.[5] The regulation of the interaction between basic oxygen species and catalytic sites was reported in previous studies to reduce the charging overpotential. Therefore, cathode catalysts generally with Lewis acidity (LA) were well developed, including carbon based materials[6], noble metals and alloys[7-12], metal chalcogenides[13-16], and metal oxides[17-20]. On the contrary, the function of Lewis basicity (LB) in the cathode catalysts on the electrochemical performance of LOBs are still underestimated.

Given the acidity of Li^+ in the discharge product Li_2O_2, it is envisaged that catalysts with Lewis basicity would interact with the acidic Li^+ to promote Li_2O_2 decomposition, and consequently improve the OER kinetics. To the best of our knowledge, only a few catalysts with Lewis basicity like metal-organic frameworks (MOFs) with amino groups were developed for LOBs so far.[21] The stability of these materials was poor and the synthetic procedures were complicated most of the time. Generally, Lewis basicity originates from electron donating ability of atoms like N, O, P, S, etc. In the catalysts based on transition metal oxides (TMOs), most are stable and convenient to synthesize, and Lewis basicity could also be generated with the presence of oxygen atoms with electron donating properties.[22] However, intrinsic Lewis basicity of lattice oxygen (O_L) in TMOs is poor due to the deep alignment of O *2p* band and its separation from transition metal (TM) *d* band. So, electrons in the *d* band of TM can exhibit higher donating preference than the *p*-band electrons of O_L.[23]

In order to enhance the Lewis basicity of O_L, it is necessary to adjust O *2p* band upwards in TMOs (Figure 1a). High entropy oxides (HEOs) usually refer to crystalline oxides including 5 or more cations in a single phase.[24] In HEOs, the completely random arrangement of elements leads to a broad *d* band, which could regulate the position of TM *d* band relative to O *2p* band and reduce their separation.[25, 26] Moreover, constraining various

10.1002/anie.202509132

cations with different ionic radius in a single lattice would lead to remarkable lattice distortion and further activate O_L in HEOs.[27] With flexible band and element tunability, HEOs offer us a promising chance to regulate O_L in the oxide lattice for the introduction of LB.

Herein, a new type of HEO with Lewis basicity (LB-HEO) was designed and developed as the cathode catalyst for LOBs, using Joule-heating (JH) method. Spinel oxide with two different cation sites, tetrahedral sites (Td) and octahedral sites (Oh), was selected as the structure model in this work. TMOs could be considered as the combination of a series of M-O_L-M' units as shown in Figure 1b. Due to two-site lattice in spinel oxides, all of the M-O_L-M' units in spinel oxides are M_{Td}-O_L-M_{Oh} units. It is feasible to regulate the chemical environment of O_L precisely using transition metals with different site occupation preference. Five transition metal elements (Cr, Mn, Co, Ni, Zn) were chosen to activate the O_L and generate Lewis basicity in LB-HEO. LB-HEO could interact with Li^+ in Li_2O_2 and promote the dissolution of Li^+ during OER, accelerating the kinetics of interfacial charge transfer between Li_2O_2 and cathode. As a result, the LOBs with LB-HEO showed low charge overpotential of 0.97 V, and long cycling life span of 135 cycles was achieved at 100 mA g^{-1} when capacity limited at 1000 mAh g^{-1}. This work demonstrates a new method of introducing Lewis basicity into transition metal oxides through regulation of the chemical environment of O_L, and provides a new strategy for accelerating the OER kinetics by designing high-performance catalysts that can regulate Li^+ in Li_2O_2.

Results and Discussion

Spinel oxide with tetrahedral (Td) and octahedral (Oh) sites was chosen here to construct LB-HEO. In the high entropy spinel oxides, if Td sites are exclusively occupied by specific cations, the remaining metal elements could randomly occupy the Oh sites.[28-30] By regulating the M_{Td}-O_L-M_{Oh} units (Figure 1b) through precise site occupation of particular elements, lattice oxygen (O_L) is expected to exhibit different properties. Previous studies showed that Zn^{2+} has the highest preference for Td sites in spinel oxides, whereas cations such as Cr^{3+}, Mn^{2+} or Mn^{3+}, Fe^{3+}, Co^{2+} or Co^{3+}, and Ni^{2+} or Ni^{3+} tend to occupy Oh sites. In practice, the Zn cation was selected to occupy the Td sites and Cr, Mn, Fe, Co, Ni cations were then chosen to occupy the Oh sites.[28-31] According to Figure 1a, energy of O_L *2p* electrons would increase as elements with low electronegativity are introduced.[32] This indicates a higher electron-donating ability of the O_L, corresponding to the increased Lewis basicity in the material. Among expected elements in the Oh sites (Cr, Mn, Fe, Co, Ni), low electronegative Cr (χ_{Cr} = 1.66) together with Mn, Co, Ni were chosen to generate Lewis basicity in high entropy oxide (LB-HEO). For comparison, Cr was replaced by high electronegative Fe (χ_{Fe} = 1.83) to obtain the control group (N-HEO). The HEOs were synthesized by ultra-fast Joule-heating method, wherein a direct high-temperature pulse (heating rate > 1200 K s^{-1}) was applied to the carbon clothes infiltrated with homogeneous solution. This method could prevent the significant phase separation which is typical in the traditional high-temperature solid-state synthesis associated with time-consuming diffusion process (Scheme 1).

Determined by thermogravimetric (TG) analysis, the content of HEOs on the carbon cloth was approximately 6% (Figure S1). The presence of a single spinel phase on carbon cloth was confirmed by X-ray diffraction (XRD) patterns for both LB-HEO and N-HEO in Figure 1c. The diffraction peaks at 30°, 35°, 37° and 43° are ascribed to the (220), (311), (222) and (400) planes of the spinel crystal, respectively. The scanning electron microscope (SEM) image in Figure 1d shows that HEOs with particle size of less than 100 nm are evenly distributed on the surface of carbon fiber. In the high-resolution transmission electron microscopy (HR-TEM) image of LB-HEO (Figure 1e), distinct lattice fringe with a spacing of 0.299 nm was observed, corresponding to the (220) plane of spinel structured HEO. The inset image in Figure 1e presents the selected area electron diffraction (SAED) pattern of LB-HEO. Diffraction rings indicated the polycrystalline nature of the selected area. The rings with radius of 3.41, 4.10, and 4.87 nm^{-1}, are ascribed to the (220), (222), and (400) planes of the spinel structure, respectively. The energy dispersive X-ray spectroscopy (EDS) mapping of LB-HEO (Figure 1f) revealed a uniform distribution of Cr, Mn, Co, Ni, Zn and O elements within the LB-HEO particles, the major characteristic of high entropy oxides. Additionally, the EDS mapping of C indicates that these particles are loaded on the fibers of the carbon cloth, consistent with HR-TEM image in Figure S2 where there is carbon in contact with HEOs.

Valence state and coordination environment of the metal cations were investigated by X-ray absorption fine structure (XAFS) and X-ray photoelectron spectroscopy (XPS). According to the X-ray absorption near edge structures (XANES) (Figure 2a-b), the oxidation states of Zn were +2 and the oxidation states of Mn were between +2 and +3 in both LB-HEO and N-HEO. In the XPS spectra of Zn *2p* (Figure 2g), the peaks at 1022.0 eV and 1045.1 eV are attributed to the Zn^{2+} $2p_{3/2}$ and Zn^{2+} $2p_{1/2}$, respectively, confirming that oxidation state of Zn is +2 in both samples. In the XPS spectrum of Mn *2p* of LB-HEO (Figure 2h), a prominent peak at 642 eV is deconvoluted into two distinct peaks at 641.9 eV and 645.1 eV, which were originated from Mn^{2+} $2p_{3/2}$ and Mn^{3+} $2p_{3/2}$, respectively. The similar signal was also observed in the Mn *2p* spectrum of N-HEO. These results demonstrate the existence of both Mn^{2+} and Mn^{3+}, in agreement with the XANES results. Additionally, the XPS spectra of Co *2p* (Figure S3c) and Ni *2p* (Figure S3d) indicate that the oxidation states of both Co and Ni in LB-HEO are similar with those in N-HEO.

The Fourier transformed extended X-ray absorption fine structure (FT-EXAFS) of Zn *K*-edge shows nearly the same coordination environment between Zn in two HEO samples (Figure 2c). The first-shell peak at ~ 1.5 Å represents the bond of central zinc to the nearest coordinated oxygen (Zn-O). The peaks at ~ 2.8 Å refer to the bonds of central zinc to the nearest cations both at the Oh sites (Zn-M_{Oh}) and Td sites (Zn-M_{Td}). It confirms that the Zn^{2+} in both samples are located in the Td sites of spinel lattice.[33] In the Fourier transformed EXAFS of Mn (Figure 2d), the peaks at ~ 1.5 Å is ascribed to the Mn-O bond, and the peaks at

~ 2.7 Å and ~ 3.5 Å are attributed to Mn-M_{Oh} and Mn-Zn_{Td}. This demonstrates that the Mn cations occupy the Oh sites in the spinel structure.[34-36] Co cations have a similar Oh occupation according to the corresponding FT-EXAFS in radial space (Figure S4). Cr^{3+} also occupies Oh sites because it has nearly no preference for Td sites in previous Cr-based spinels.[37] In this way, all of the site occupations are clarified and the Zn_{Td}-O-M_{Oh} configuration is confirmed in both LB-HEO and N-HEO, in agreement with Figure 1b. According to Figure 2i, nearly overlapped *K*-edge oscillation curves of Zn, Mn and Co are obtained in two samples, indicating similar chemical environment in LB-HEO and N-HEO again. In the wavelet transform-EXAFS in Figure 2e-f, the shorter metal-oxygen bond length in LB-HEO is clearly observed, as marked with dashed lines. This indicates more overlap between TM *3d* band and O *2p* band in LB-HEO.[34, 38] Therefore, the separation of *2p* band from 3*d* band is reduced, and O *2p* electrons could then exhibit more possible electron donating ability in LB-HEO. The overall XAFS results demonstrate that higher Lewis basicity of O_L in LB-HEO is obtained by introducing elements with low electronegativity and increasing the energy of *2p* electrons.

To evaluate the catalytic activity for cathode OER of the as-prepared LB-HEO, a series of electrochemical tests were carried out on LOBs with LB-HEO, N-HEO and Super P as cathode catalyst. In the cyclic voltammograms (CV) curves with a scan rate of 0.5 mV s^{-1} (Figure 3a), the first oxidation peaks in the batteries with LB-HEO, N-HEO and Super P carbon are at the potential of 3.15 V, 3.20 V, 3.17 V (vs. Li/Li^+), respectively. This oxidation peak is ascribed to the reaction in equation 1,

$$Li_2O_2 \rightarrow Li_{2-x}O_2 + x\,e^- + x\,Li^+ \ (0 < x \leq 1) \qquad (1)$$

The higher current response of LOBs with LB-HEO is attributed to higher catalytic activity to this oxidation reactions, indicating a faster delithiation kinetics.[39-43] Tafel analysis of the oxidation peaks at about 3.2 V in Figure 3a is shown in Figure 3b. The Tafel slope of the battery with LB-HEO is 162.4 mV dec^{-1}, much lower than that of the battery with N-HEO (313.3 mV dec^{-1}) or Super P (287.4 mV dec^{-1}), suggesting a much faster OER kinetics of the LB-HEO cathode. The galvanostatic charge-discharge (GCD) profiles of LOBs with different cathode materials is shown in Figure 3c. Batteries based on LB-HEO showed the highest discharge specific capacity (~ 2000 mAh g^{-1}) and minimum charge overpotential (0.97 V) at 50 mA g^{-1}. For the batteries with N-HEO or Super P, the specific capacities are only approximately 1000 mAh g^{-1} and the charging overpotentials are 1.28 V and 1.44 V, respectively, much higher than that of batteries with LB-HEO. The difference in overpotential indicates the superior catalytic activity of LB-HEO, while N-HEO or Super P could not promote the OER process. To figure out how high entropy effect affects the catalytic activities of LB-HEO, low entropy spinels of $ZnCr_2O_4$ and $ZnFe_2O_4$ were also synthesized through the same procedure. Related GCD profiles of LOBs with those cathode materials are shown in Figure S5. Batteries with these low entropy spinel oxides only showed specific capacity less than 1000 mAh g^{-1}, and the overpotential of charging process exceeded 1.2 V, which indicates high entropic Oh sites could play an important role in the catalytic activity of LB-HEO.

The cycling stability of LOBs was also evaluated by GCD with a cutoff capacity of 1000 mAh g^{-1} and a current density of 100 mA g^{-1} (Figure 3d-e and Figure S6a). Batteries with N-HEO and Super P reached a cutoff charging voltage of 4.5 V (vs. Li/Li^+) after only 50 cycles, while batteries with LB-HEO can still cycle for 700 hours more with overpotential less than 1.4 V. When the charging overpotential of the battery with LB-HEO increased to 1.4 V significantly after approximately 90 cycles, lithium anodes were found to be seriously degraded (inset of Figure 3d and Figure S6b). A new lithium plates were then replaced for the batteries and the charging overpotential recovered to the initial value of 0.98 V. It indicates that the degradation of the battery is mainly caused by the unprotected lithium anode, and the stability of LB-HEO cathode is sufficient for long cycling test. After replaced with new lithium plate, the battery showed slow degeneration again and ultimately exhibited an improved life-span of 135 cycles. Rate performance was evaluated with a cutoff capacity of 1000 mAh g^{-1} (Figure 3f). At the current densities of 50, 100, 250, and 500 mA g^{-1}, LOBs with LB-HEO exhibited charging potentials of 3.90, 4.05, 4.16, and 4.23 V, corresponding to overpotentials of 0.94, 1.09, 1.20, and 1.27 V, respectively. After 20 cycles, the overpotential decreased to 1.03 V when the current density was set back to 50 mA g^{-1}. There is no noteworthy overpotential augmentation during the 5 cycles at each current density. Accordingly, LB-HEO could effectively improve the cycling stability of LOBs, attributed to lower overpotential during charging process that prohibits the degradation of the cathode materials and the side reaction of the electrolyte.

To further understand the improved electrochemical performance of LOBs with LB-HEO cathode, interfacial charge transfer kinetics was investigated by temperature-dependent electrochemical impedance spectrums (EIS). According to fitting data in Figure S9, related distribution of relaxation time (DRT) coupled with temperature was obtained for both LB-HEO (Figure 4a) and N-HEO (Figure 4b). The strong signals in the range of 10^{-3} - 10^{-2} s are attributed to interfacial charge transfer resistance at Li_2O_2|cathode interface. The signals moved towards high frequency region as temperature rises, indicating lowered resistance for interfacial charge transfer at higher temperature. Signals at 10^{-6} and 10^{-4} s are ascribed to the overall ohmic resistance of the batteries and solid-electrolyte interface (SEI) formation, respectively.[44-47] There is no temperature dependence for ohmic resistance, which is electrical response instead of chemical behavior, in accordance with previous DRT study about lithium-ion battery system.[48] Based on the signals at 10^{-3} - 10^{-2} s, the activation energy (E_a) of the interfacial charge transfer could be calculated by linear fitting of ln(R_{ct}) versus T^{-1} according to the Arrhenius equation 2,

$$1/R_{ct} = A \cdot e^{-\frac{E_a}{RT}} \qquad (2)$$

where the E_a is activation energy of the interfacial charge transfer, R_{ct} is interfacial charge transfer resistance, T is Kelvin thermodynamic scale of temperature, R is universal gas constant and A is pre-exponential factor. The E_a in LOBs with LB-HEO is 22.4 kJ mol^{-1}, three times smaller than that of the LOBs with N-HEO (63.5 kJ mol^{-1}), which shows much faster kinetic in the batteries with LB-HEO. The EIS and DRT results demonstrate

10.1002/anie.202509132

that the superior electrochemical performance of LOBs with LB-HEO cathode originates from the fast charge transfer kinetics at the LB-HEO|Li_2O_2 interface.

Potentiostatic intermittent titration technique (PITT) was then applied to explore the influence of the Lewis basicity on the discharge product, Li_2O_2, at the LB-HEO|Li_2O_2 interfaces. As one of the intermittent titration methods for transient state of system, PITT can reveal chemical diffusion kinetics of specific ions in materials.[49, 50] Figure 4d shows the PITT voltage and current curves during the charging process after a complete discharging on the LOBs with LB-HEO and N-HEO cathodes. The step voltage applied during the PITT process started at 2.8 V, increasing by 0.02 V per step, and the cutoff current was 1 μA for each titration step. Prior to reaching 3.8 V, the voltage curve consists of many short-duration constant potential plateaus, exhibiting a staircase-like rise. Once the voltage reached 3.8 V, the voltage curve transited into a long plateau with a constant potential. These two distinct voltage ranges are attributed to the lithium ion extraction process and the bulk phase oxidation process of Li_2O_2, respectively[39], corresponding to the two oxidation peaks at 3.2 V and 4.0 V in the CV curves (Figure 3a). During the lithium ion extraction process (2.8 - 3.8 V), each constant potential step triggered a "pulse-relaxation" current response in the current curve, representing an titration process at constant potential. In the bulk phase oxidation process (3.8 V), the long voltage plateau indicates the ongoing oxidation reaction, during which the current consistently remained above the cutoff current (1 μA).

Based on the current profiles, the chemical diffusion coefficient ($\tilde{\boldsymbol{D}}$) of Li^+ in Li_2O_2 at different steps of PITT was calculated according to electrochemical diffusion differential equations to understand the delithiation process (Figure 4e). Two repeated measurements were conducted and similar PITT results were obtained. As the charging potential increases in PITT tests, the variation tendency of the $\tilde{\boldsymbol{D}}$ value could reveal the Li^+ behavior in Li_2O_2. $\tilde{\boldsymbol{D}}$ in the batteries with N-HEO ($\tilde{\boldsymbol{D}}_{\boldsymbol{N}}$, red dots in Figure 4e) firstly decreased to 10^{-18} cm^2 s^{-1}, then gradually increased to 10^{-16} cm^2 s^{-1} during the charging potential of 3.0 - 3.5 V until another declination arose over 3.5 V. The first downslope is attributed to the higher activation energy for Li^+ in the ordered Li_2O_2 hopping between lattice sites during delithiation. When $\tilde{\boldsymbol{D}}_{\boldsymbol{N}}$ decreased to the minima at 3.0 V, Li_2O_2 then transited into disordered Li_2O_2 due to the generation of more Li^+ vacancy in the lattice of Li_2O_2. The disorder increases and the activation energy of Li^+ hopping in the lattice reduces when higher overpotential is applied, leading to the increasing $\tilde{\boldsymbol{D}}_{\boldsymbol{N}}$ from 10^{-18} cm^2 s^{-1} to 10^{-16} cm^2 s^{-1} at 3.0 - 3.5 V. The second downslope over 3.5 V is due to the gradual Li^+ depletion in Li_2O_2. These variation trends in $\tilde{\boldsymbol{D}}_{\boldsymbol{N}}$ are consistent with Li^+ transportation behavior in the intercalation cathode materials like $LiCoO_2$.[51, 52] In comparison, the overall value of $\tilde{\boldsymbol{D}}$ in the batteries with LB-HEO ($\tilde{\boldsymbol{D}}_{\boldsymbol{LB}}$, blue dots in Figure 4e) is about two order of magnitude higher than that in the batteries with N-HEO. This result indicates the lower activation and faster kinetics for delithiation in LOBs with LB-HEO during charging process. In addition, the phenomenon of increasing $\tilde{\boldsymbol{D}}_{\boldsymbol{LB}}$ was absent in the potential range of 3.0 - 3.5 V, in which the $\tilde{\boldsymbol{D}}_{\boldsymbol{LB}}$ remained at around 10^{-16} cm^2 s^{-1}. It indicates that the disorder within Li_2O_2 in batteries with LB-HEO at 3.0 V is more significant than that in batteries with N-HEO, and further activation under high overpotential (3.0 - 3.5 V) is not necessary for Li^+ hopping and delithiation. The analyses on the PITT data demonstrate that Lewis basicity in LB-HEO can effectively introduce more disorder in Li_2O_2 through the Lewis base-acid interaction between basic sites and Li^+ in Li_2O_2. This disorder in Li_2O_2 could facilitate the delithiation kinetics, and then contributed to the superior interfacial charge transfer kinetics and improved performance in LOBs with LB-HEO.

To further investigate the disorder in Li_2O_2 as indicated by the PITT tests, XPS depth profiling was employed to examine the chemical environment of Li_2O_2 at the cathode surface of LOBs with LB-HEO after a complete discharging. Etching with an argon ion beam (Ar^+), the signal intensities of O and Li progressively diminished (Figure 4f), indicating the etching of Li_2O_2 from the surface of carbon fibers. In the XPS spectra of O 1s (Figure 4g), the peaks at 530 eV and 532 eV are attributed to the delithiated discharge product $Li_{2-x}O_2$ and the stoichiometric discharge product Li_2O_2, respectively. The relative intensity ratio of the 530 eV peak to the 532 eV peak increases from 0 to 0.97 with the etching time. In the XPS spectra of Li 1s (Figure 4h), the peak at 55 eV that is corresponding to Li_2O_2 gradually shifts to higher binding energies, suggesting more Li^+ vacancies in Li_2O_2 when approaching the LB-HEO|Li_2O_2 interface.[53, 54] These XPS results clearly indicate that the disorder observed in the PITT tests is attributed to the delithiated discharge product $Li_{2-x}O_2$, and more delithiated species are generated near the LB-HEO|Li_2O_2 interface.

Based on the analyses on the PITT and XPS data, the mechanism by which LB-HEO enhances oxygen conversion kinetics through its Lewis basicity is proposed. Upon discharging, Li_2O_2 is deposited on LB-HEO, and the basic sites on LB-HEO attract Li^+ ions from Li_2O_2, initially forming an electrochemically active layer of $Li_{2-x}O_2$ at the LB-HEO|Li_2O_2 interface. During the early stage of the delithiation in the charging process, Li^+ can easily migrate from the nearby Li_2O_2 to the $Li_{2-x}O_2$ without requiring a high overpotential, and eventually dissolves into the electrolyte. This leads to the accumulation of $Li_{2-x}O_2$ from the LB-HEO|Li_2O_2 interface to the Li_2O_2|electrolyte interface by the end of the delithiation process. Subsequently, bulk oxidation occurs in $Li_{2-x}O_2$ at a low overpotential, facilitating the transformation of the discharge product into O_2. This oxidation process could also be supported by isotopic labeling which found that Li_2O_2 oxidation started from the surface area without interfacial contact loss.[55]

To elucidate how Lewis basicity of the activated O_L is exhibited in LB-HEO, a CO_2 quenching experiment was conducted on LB-HEO@CC (Figure 5a). Due to the intrinsic Lewis acidity of carbon in CO_2, it is theoretically expected that the Lewis basic sites of LB-HEO will be occupied by CO_2 during the quenching process. In comparison with acidic Li^+, CO_2 could not only show Lewis acidity but its interaction with basic sites can also be effectively determined by many spectroscopy methods. This offers the chance to simulate the Lewis base-acid interaction between LB-HEO and Li^+. Raman spectroscopy was used to confirm the presence of CO_2 molecules at the LB-HEO surface. As shown in Figure 5b, the Raman spectra of LB-HEO@CC before (LB-HEO) and after (Q-LB) the quenching process display prominent peaks around 1340 cm^{-1} and 1601 cm^{-1}, corresponding

10.1002/anie.202509132

to the D band and G band of carbon cloth, respectively. Compared with the LB-HEO spectrum, the Q-LB spectrum features an additional peak near 1525 cm^{-1}, which is attributed to chemisorbed carbon dioxide (CO_2*).[56-58] In contrast, the Raman spectrum of N-HEO@CC after CO_2 quenching (Q-N) does not show a peak in this wavenumber range, indicating that no significant amount of CO_2 is chemisorbed by N-HEO. The distinct difference between the Raman spectra of Q-LB and Q-N provides strong evidence for the existence of Lewis basicity in LB-HEO, consistent with the EXAFS analyses. The configuration of CO_2* was further investigated by microscopic FT-IR in the attenuated total reflection mode (ATR-IR) (Figure 5c). Signals at 1726 cm^{-1} and 1716 cm^{-1} are attributed to HCO_3^- structures, while signals at 1654 cm^{-1} and 1640 cm^{-1} are associated with bidentate HCO_3^-. The signals at 1546 cm^{-1} and 1438 cm^{-1} are assigned to bidentate CO_3^{2-} and polydentate CO_3^{2-}, respectively.[59] These signals provide direct evidence of the interaction between O_L and the carbon site of CO_2, further confirming the Lewis basicity of activated O_L sites in LB-HEO.

The GCD profile of LOBs with the Q-LB cathode was also acquired (Figure 5d). The specific capacity of LOBs with Q-LB was reduced by more than 50%, and the OER overpotential increased to 1.23 V. The electrochemical performance of the batteries with the Q-LB cathodes is far inferior to that of the batteries with pristine LB-HEO cathodes, clearly demonstrating that the electrochemical catalytic activity of LB-HEO is strongly correlated with its Lewis basic sites and aligning with the findings from EIS and PITT data.

Density functional theory (DFT) calculation was performed to better understand electronic structure in LB-HEO. The projected density of states (p-DOS) for lattice oxygen of LB-HEO and N-HEO are presented in Figure 5e. For the O *2p* band of LB-HEO between energy of -0.5 and 0 eV (vs. Fermi level, i.e., E_F), there is a higher electron density near the Fermi level compared with the O 2p band of N-HEO, where the electron density is predominantly located between -2 and -0.5 eV (vs. E_F). This result indicates that the O *2p* band in LB-HEO shifts towards Fermi level, which is due to the lower electronegativity of Cr in LB-HEO compared with that of Fe in N-HEO. This shift is consistent with previous researches showing an increasing in the energy of *2p* band.[32] The DFT results demonstrate that the lattice oxygens in LB-HEO become more activated, exhibiting a greater electron-donating characteristic and enhanced Lewis basicity, which further supports our discussion based on EXAFS and electrochemical measurements.

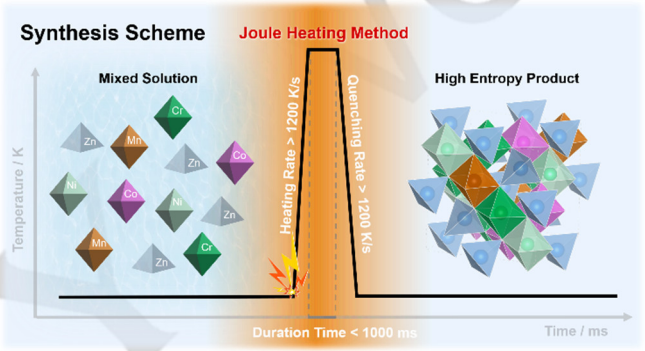

Scheme 1. Schematic illustration of the preparation of HEOs with Joule Heating method.

10.1002/anie.202509132

RESEARCH ARTICLE

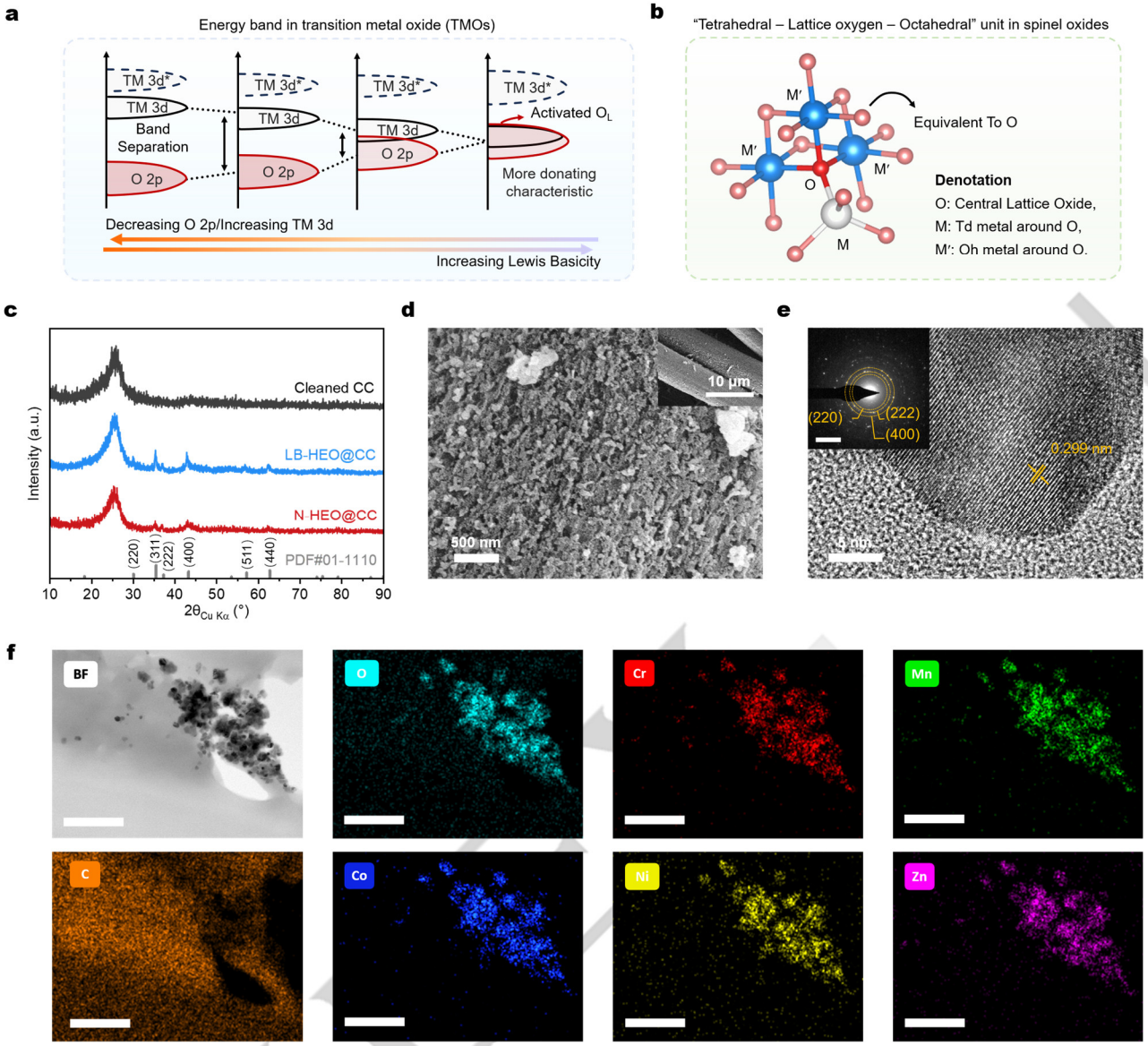

Figure 1. (a) Schematic explanation of correlation between Lewis basicity and band theory. (b) Schematic diagram of a M_{Oh}-O-M_{Td} unit in the two-site spinel oxides. (c) XRD spectra of carbon cloth, LB-HEO and N-HEO. (d) SEM image of LB-HEO on carbon cloth (inset: SEM image of a lower resolution). (e) HR-TEM image of LB-HEO (inset: SAED pattern of LB-HEO with scale bar of 5 nm^{-1}). (f) EDS mappings of LB-HEO with scale bar of 200 nm. Panels labelled as C, O, Cr, Mn, Co, Ni and Zn are EDS mappings of corresponding elements.

10.1002/anie.202509132

RESEARCH ARTICLE

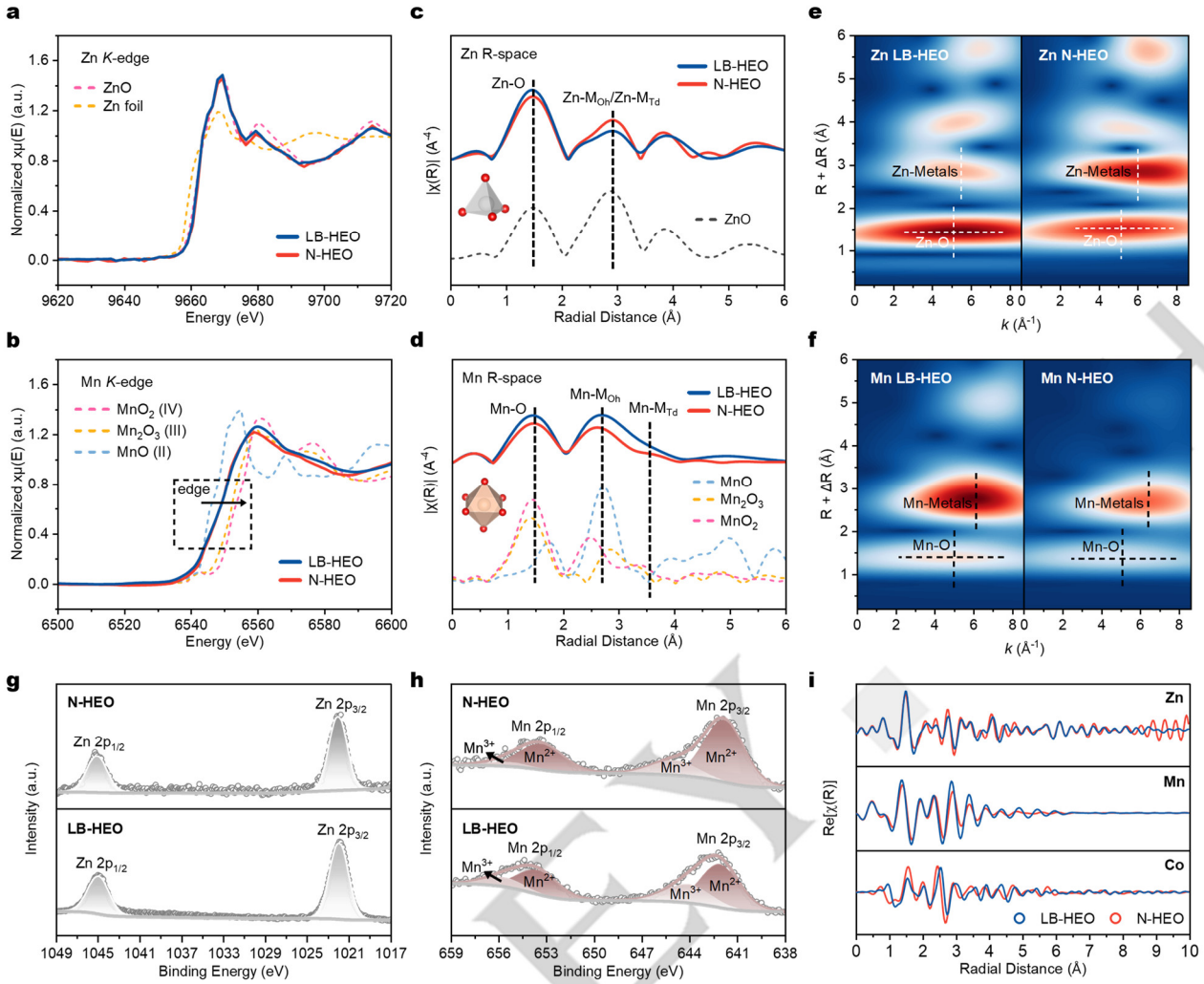

Figure 2. Normalized *K*-edge XANES spectra of (a) Zn and (b) Mn. k^3-weighted Fourier transform EXAFS spectra of (c) Zn and (d) Mn. Wavelet transform EXAFS spectra of (e) Zn and (f) Mn. XPS spectra of (g) Zn *2p*, (h) Mn *2p*. (i) Real part of all Fourier transform EXAFS spectra.

10.1002/anie.202509132

RESEARCH ARTICLE

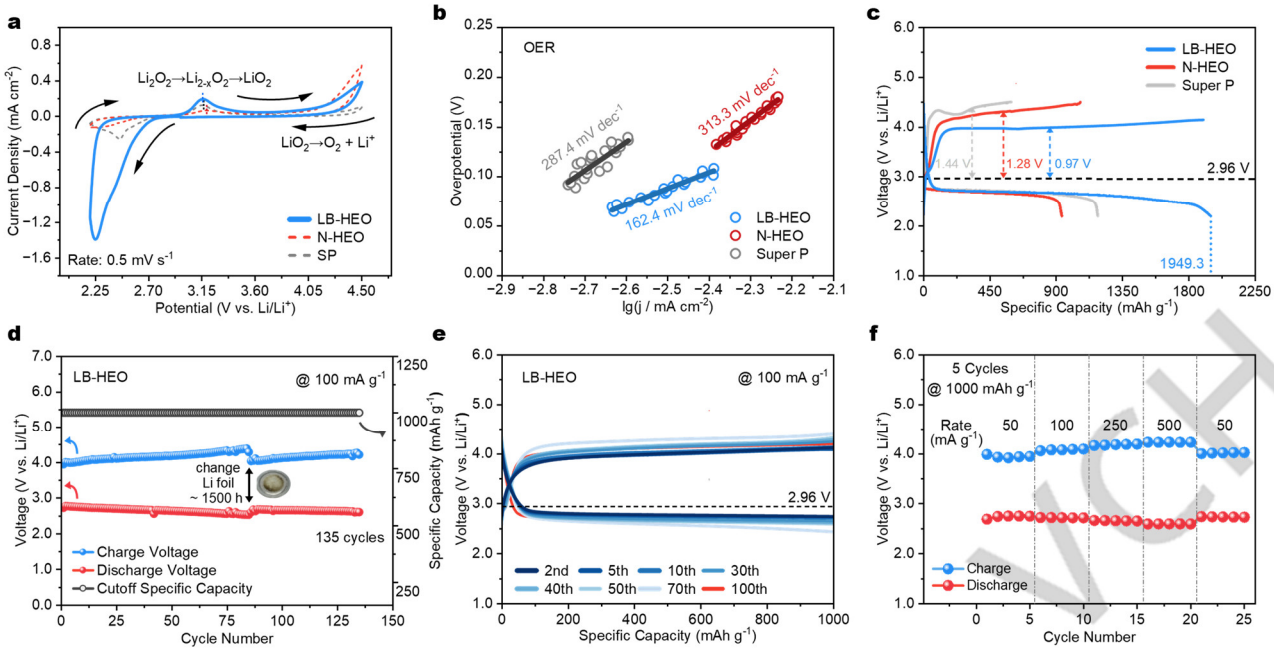

Figure 3. (a) CV tests of LB-HEO, N-HEO and Super P. (b) Tafel analysis of OER peak in CV curves. (c) Initial full discharge-charge curves of LOBs with different catalysts loaded on cathodes. (d)-(e) Cycling performance and representative discharge/charge profiles of LOBs with LB-HEO at 100 mA g^{-1} with capacity limitation of 1000 mAh g^{-1}. (f) Rate performance of LOBs with LB-HEO catalyst.

10.1002/anie.202509132

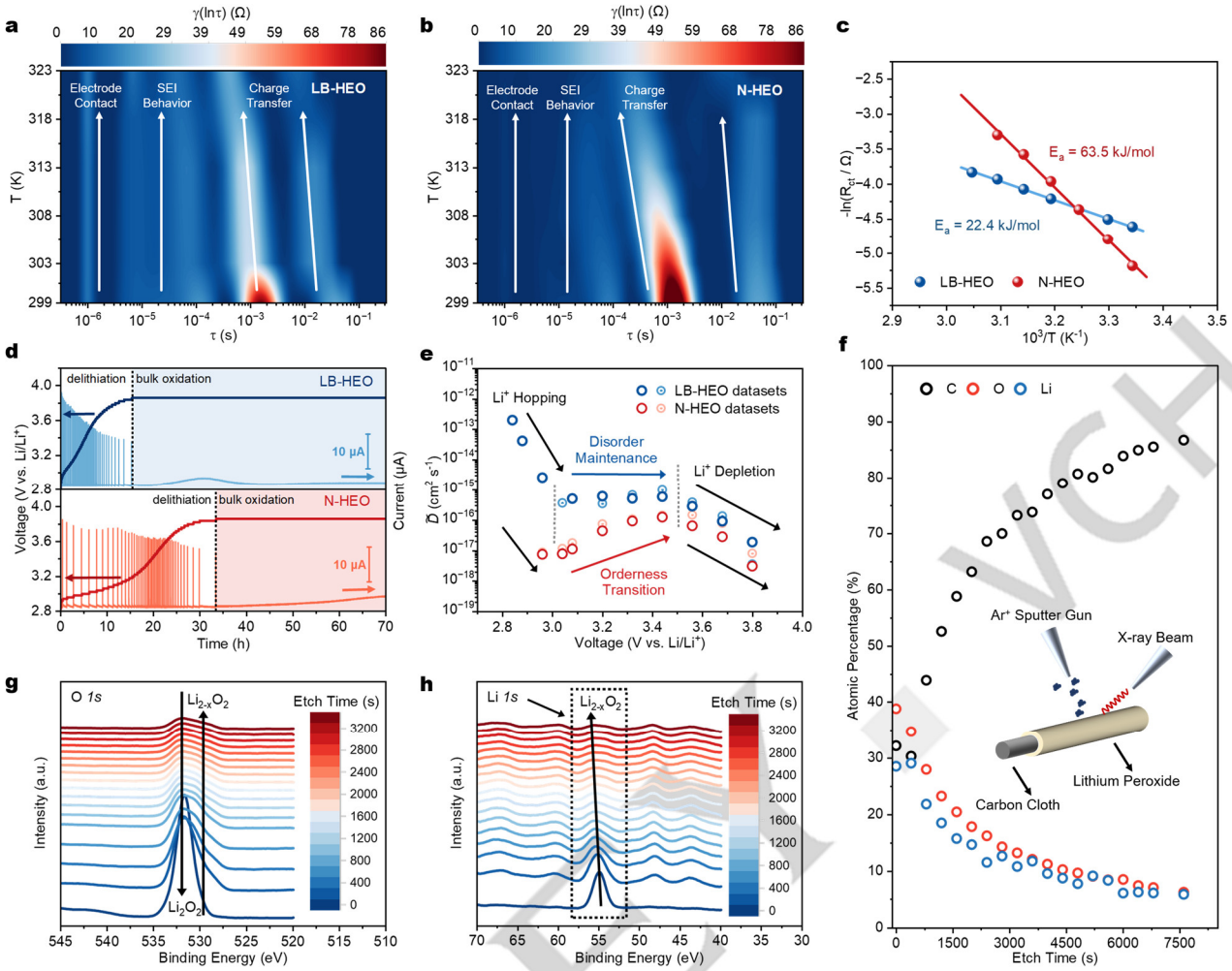

Figure 4. Temperature-dependent EIS tests and related DRT analysis of (a) LB-HEO and (b) N-HEO. (c) Arrhenius behavior fitting of interfacial charge transfer resistance. (d) The variation of current and voltage of LOBs with LB-HEO and N-HEO as catalysts with charge time in PITT tests. (e) The repeated chemical diffusion coefficient of Li^+ at different charge voltage. (f) Related atomic percentage of etched compounds during XPS depth profiling (inset: schematic diagram of depth profiling test). (g) O *1s* and (h) Li *1s* XPS depth profiling of discharge product on LB-HEO.

10.1002/anie.202509132

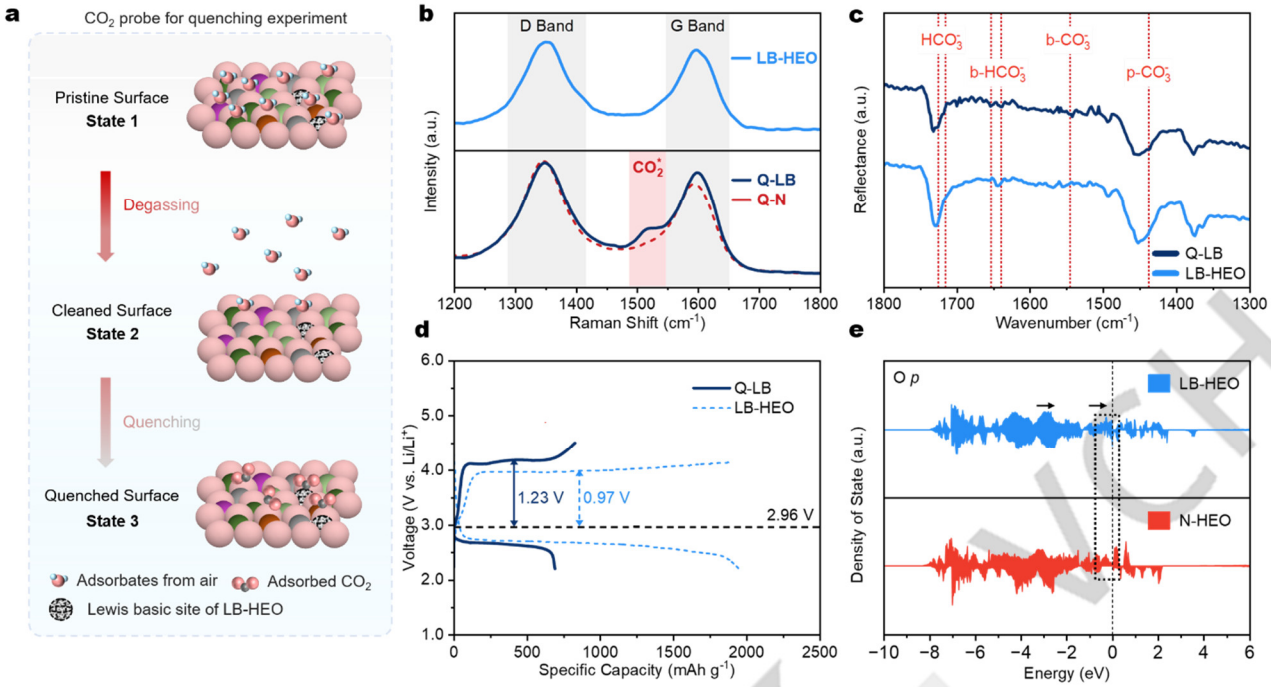

Figure 5. (a) Schematic diagram of CO_2-quenching process. (b) Raman spectra of LB-HEO, Q-LB and Q-N. (c) FT-IR spectra of LB-HEO and Q-LB. (d) Comparison of initial full discharge-charge curves of LOBs with LB-HEO and Q-LB as catalysts. (e) PDOS of oxygen *p* band in LB-HEO and N-HEO.

Conclusion

In summary, Lewis basicity was introduced into HEO through O_L activation, resulting excellent catalytic performance for the OER at the cathode of LOBs. Characterized with XRD, TEM and XAFS, as-prepared HEOs were spinel oxides with precise control of cation occupation in Td and Oh sites. Lewis basicity was confirmed in the O_L of LB-HEO by XAFS and CO_2 quenching experiment with Raman and FT-IR spectroscopy. In LOBs with LB-HEO as cathode catalyst, the DRT results derived from EIS indicated the improvement of interfacial charge transfer kinetics. The PITT and XPS depth profiles further demonstrated that the improved interfacial charge transfer kinetics originated from the facilitated delithiation process through Lewis acid-base interaction between LB-HEO and Li^+ in Li_2O_2, which resulted in more disordered discharge product with Li^+ defects. As a result, the LOBs showed a low overpotential of 0.97 V, and a long-term stability for 135 cycles with a capacity of 1000 mAh g^{-1} at 100 mA g^{-1}. This work paved a novel pathway for understanding the catalytic activity of high entropy oxide. It also showed that Li^+ activation plays an important role in OER, prompting further exploration in the future.

Supporting Information

The authors have cited additional references within the Supporting Information.[39, 45, 60-64]

Acknowledgements

This work was financially supported by National Key R&D Program of China (2023YFA1506300), National Natural Science Foundation of China (22475127, 22133005), Shanghai Municipal Science and Technology Major Project, and Zhiyuan Future Scholar Program (ZIRC2023-09).

Keywords: Lewis Basicity • Li_2O_2 Disorder • Interfacial Charge Transfer Kinetics • Lithium-Oxygen Battery • High Entropy Oixde

[1] K. Wang, Q. Zhu, J. Chen, *Small* **2018**, *14*, e1800078.
[2] T. Liu, J. P. Vivek, E. W. Zhao, J. Lei, N. Garcia-Araez, C. P. Grey, *Chem. Rev.* **2020**, *120*, 6558-6625.
[3] Y. Zhou, S. Guo, *eScience* **2023**, *3*, 100123-100138.
[4] B. Wen, Z. Zhu, F. Li, *Journal of Electrochemistry* **2023**, *29*, 2215001-2215013.
[5] Y. Zhou, K. Yin, Q. Gu, L. Tao, Y. Li, H. Tan, J. Zhou, W. Zhang, H. Li, S. Guo, *Angew. Chem. Int. Ed.* **2021**, *60*, 26592-26598.
[6] S. Xu, X. Liang, Z. Ren, K. Wang, J. Chen, *Angew. Chem. Int. Ed.* **2018**, *57*, 6825-6829.
[7] S. Yang, Y. Qiao, P. He, Y. Liu, Z. Cheng, J. Zhu, H. Zhou, *Energy Environ. Sci.* **2017**, *10*, 972-978.
[8] X. Hu, G. Luo, Q. Zhao, D. Wu, T. Yang, J. Wen, R. Wang, C. Xu, N. Hu, *J. Am. Chem. Soc.* **2020**, *142*, 16776-16786.
[9] L. Song, W. Zhang, Y. Wang, X. Ge, L. Zou, H. Wang, X. Wang, Q. Liu, F. Li, J. Xu, *Nat. Commun.* **2020**, *11*, 2191.

[10] P. Wang, Y. Ren, R. Wang, P. Zhang, M. Ding, C. Li, D. Zhao, Z. Qian, Z. Zhang, L. Zhang, L. Yin, *Nat. Commun.* **2020**, *11*, 1576.
[11] L. Liu, C. Zhou, W. Fang, Y. Hou, Y. Wu, *Energy Mater.* **2023**, *3*, 300011-300020.
[12] W. Zhang, J. Chang, Y. Yang, *SusMat* **2023**, *3*, 2-20.
[13] X. Mu, C. Xia, B. Gao, S. Guo, X. Zhang, J. He, Y. Wang, H. Dong, P. He, H. Zhou, *Energy Storage Mater.* **2021**, *41*, 650-655.
[14] X. Han, L. Zhao, Y. Liang, J. Wang, Y. Long, Z. Zhou, Y. Zhang, Y. Li, J. Ma, *Adv. Energy Mater.* **2022**, *12*, 2202747.
[15] S. Li, Y. Liu, X. Wu, K. Wang, J. Chen, *Small* **2023**, *19*, 2304435.
[16] Y. Pan, C. Zhao, A. Hu, R. Li, B. Zhou, Y. Fan, J. Chen, Z. Yan, C. Su, J. Long, *J. Colloid Interface Sci.* **2023**, *635*, 138-147.
[17] J. Li, M. Zou, W. Wen, Y. Zhao, Y. Lin, L. Chen, H. Lai, L. Guan, Z. Huang, *J. Mater. Chem. A* **2014**, *2*, 10257.
[18] X. Cao, J. Wu, C. Jin, J. Tian, P. Strasser, R. Yang, *ACS Catal.* **2015**, *5*, 4890-4896.
[19] T.-H. Gu, D. A. Agyeman, S.-J. Shin, X. Jin, J. M. Lee, H. Kim, Y.-M. Kang, S. J. Hwang, *Angew. Chem. Int. Ed.* **2018**, *57*, 15984-15989.
[20] Y. Li, J. Qin, Y. Ding, J. Ma, P. Das, H. Liu, Z. Wu, X. Bao, *ACS Catal.* **2022**, *12*, 12765-12773.
[21] C. Zhao, Z. Yan, B. Zhou, Y. Pan, A. Hu, M. He, J. Liu, J. Long, *Angew. Chem. Int. Ed.* **2023**, *62*, e202302746.
[22] P. C. Stair, *J. Am. Chem. Soc.* **1982**, *104*, 4044-4052.
[23] N. Zhang, Y. Chai, *Energy Environ. Sci.* **2021**, *14*, 4647-4671.
[24] C. M. Rost, E. Sachet, T. Borman, A. Moballegh, E. C. Dickey, D. Hou, J. L. Jones, S. Curtarolo, J. P. Maria, *Nat. Commun.* **2015**, *6*, 8485.
[25] H. Wu, Q. Lu, Y. Li, J. Wang, Y. Li, R. Jiang, J. Zhang, X. Zheng, X. Han, N. Zhao, J. Li, Y. Deng, W. Hu, *Nano Lett.* **2022**, *22*, 6492-6500.
[26] R. R. Katzbaer, F. M. dos Santos Vieira, I. Dabo, Z. Mao, R. E. Schaak, *J. Am. Chem. Soc.* **2023**, *145*, 6753-6761.
[27] J. Baek, M. D. Hossain, P. Mukherjee, J. Lee, K. T. Winther, J. Leem, Y. Jiang, W. C. Chueh, M. Bajdich, X. Zheng, *Nat. Commun.* **2023**, *14*, 5936.
[28] J. Wu, X. Wang, W. Zheng, Y. Sun, Y. Xie, K. Ma, Z. Zhang, Q. Liao, Z. Tian, Z. Kang, Y. Zhang, *J. Am. Chem. Soc.* **2022**, *144*, 19163-19172.
[29] C. Zhang, X. Lu, X. Han, J. Yu, C. Zhang, C. Huang, L. Balcells, A. G. Manjon, J. Jacas Biendicho, J. Li, J. Arbiol, G. Sun, J. Y. Zhou, A. Cabot, *J. Am. Chem. Soc.* **2023**, *145*, 18992-19004.
[30] Q. Hu, S. Qi, Q. Huo, Y. Zhao, J. Sun, X. Chen, M. Lv, W. Zhou, C. Feng, X. Chai, H. Yang, C. He, *J. Am. Chem. Soc.* **2023**, *146*, 2967-2976.
[31] C. Triolo, S. Schweidler, L. Lin, G. Pagot, V. Di Noto, B. Breitung, S. Santangelo, *Energy Adv.* **2023**, *2*, 667-678.
[32] Z. Huang, J. Song, Y. Du, S. Xi, S. Dou, J. M. V. Nsanzimana, C. Wang, Z. J. Xu, X. Wang, *Nat. Energy* **2019**, *4*, 329-338.
[33] Yi Huang, Song Lin Zhang, Xue Feng Lu, Zhi-Peng Wu, Deyan Luan, X. W. D. Lou, *Angew. Chem. Int. Ed.* **2021**, *60*, 11841-11846.
[34] S. Sun, Y. Sun, Y. Zhou, S. Xi, X. Ren, B. Huang, H. Liao, L. P. Wang, Y. Du, Z. J. Xu, *Angew. Chem. Int. Ed.* **2019**, *58*, 6042-6047.
[35] H. Zhao, L. Zhu, J. Yin, J. Jin, X. Du, L. Tan, Y. Peng, P. Xi, C. Yan, *Angew. Chem. Int. Ed.* **2024**, *63*, e202402171.
[36] G. Zhang, J. Pei, Y. Wang, G. Wang, Y. Wang, W. Liu, J. Xu, P. An, H. Huang, L. Zheng, S. Chu, J. Dong, J. Zhang, *Angew. Chem. Int. Ed.* **2024**, *63*, e202407509.
[37] J. Sun, H. Xue, Y. Zhang, X. Zhang, N. Guo, T. Song, H. Dong, Y. Kong, J. Zhang, Q. Wang, *Nano Lett.* **2022**, *22*, 3503-3511.
[38] Z. Yin, Y. Huang, K. Song, T. Li, J. Cui, C. Meng, H. Zhang, J. Wang, *J. Am. Chem. Soc.* **2024**, *146*, 6846-6855.
[39] B. M. Gallant, D. G. Kwabi, R. R. Mitchell, J. Zhou, C. V. Thompson, Y. Shao-Horn, *Energy Environ. Sci.* **2013**, *6*, 2518-2528.
[40] S. Kang, Y. Mo, S. P. Ong, G. Ceder, *Chem. Mater.* **2013**, *25*, 3328-3336.
[41] S. Xu, X. Liang, X. Wu, S. Zhao, J. Chen, K. Wang, J. Chen, *Nat. Commun.* **2019**, *10*, 5810.
[42] W. Bai, Z. Zhang, K. Wang, J. Chen, *Battery Energy* **2022**, *1*, 20220019.
[43] R. Zheng, D. Du, Y. Yan, S. Liu, X. Wang, C. Shu, *Adv. Funct. Mater.* **2024**, *34*, 2316440.
[44] C. Shu, C. Wu, J. Long, H. Guo, S. Dou, J. Wang, *Nano Energy* **2019**, *57*, 166-175.
[45] Y. Lu, C. Zhao, J. Huang, Q. Zhang, *Joule* **2022**, *6*, 1172-1198.
[46] R. Soni, J. B. Robinson, P. R. Shearing, D. J. L. Brett, A. J. E. Rettie, T. S. Miller, *Energy Storage Mater.* **2022**, *51*, 97-107.
[47] J. Chen, E. Quattrocchi, F. Ciucci, Y. Chen, *Chem* **2023**, *9*, 2267-2281.
[48] J. P. Schmidt, T. Chrobak, M. Ender, J. Illig, D. Klotz, E. Ivers-Tiffée, *J. Power Sources* **2011**, *196*, 5342-5348.
[49] C. Delacourt, M. Ati, J. M. Tarascon, *J. Electrochem. Soc.* **2011**, *158*, A741-A749.
[50] Y. Lv, M. Zhao, Y. Du, Y. Kang, Y. Xiao, S. Chen, *Energy Environ. Sci.* **2022**, *15*, 4748-4760.
[51] Young-Il Jang, Bernd J. Neudecker, N. J. Dudney, *Electrochem. Solid-State Lett.* **2001**, *4*, A74-A77.
[52] H. Xia, L. Lu, G. Ceder, *J. Power Sources* **2006**, *159*, 1422-1427.
[53] G. Li, N. Li, S. Peng, B. He, J. Wang, Y. Du, W. Zhang, K. Han, F. Dang, *Adv. Energy Mater.* **2020**, *11*, 2002721.
[54] H. Huang, C. Cheng, G. Zhang, L. Guo, G. Li, M. Pan, F. Dang, X. Mai, *Adv. Funct. Mater.* **2022**, *32*, 2111546.
[55] Y. Wang, Y. Lu, *Angew. Chem. Int. Ed.* **2019**, *58*, 6962-6966.
[56] Y. Zhao, X. Zhang, N. Bodappa, W. Yang, Q. Liang, P. M. Radjenovica, Y. Wang, Y. Zhang, J. Dong, Z. Tian, J. Li, *Energy Environ. Sci.* **2022**, *15*, 3968.
[57] J. Duan, T. Liu, Y. Zhao, R. Yang, Y. Zhao, W. Wang, Y. Liu, H. Li, Y. Li, T. Zha, *Nat. Commun.* **2022**, *13*, 2039.
[58] J. Liu, Z. Jiang, S. Hsu, *ACS Appl. Mater. Interfaces* **2023**, *15*, 6716-6725.
[59] I. M. Hill, S. Hanspal, Z. D. Young, R. J. Davis, *J. Phys. Chem. C* **2015**, *119*, 9186-9197.
[60] B. Ravel, M. Newville, *J. Synchrotron Radiat.* **2005**, *12*, 537-541.
[61] J. P. Perdew, K. Burke, M. Ernzerhof, *Phys. Rev. Lett.* **1996**, *77*, 3865-3868.
[62] G. Kresse, J. Furthmüller, *Comput. Mater. Sci.* **1996**, *6*, 15-50.
[63] T. Wan, M. Saccoccio, C. Chen, F. Ciucci, *Electrochim. Acta* **2015**, *184*, 483-499.
[64] F. Ciucci, *Curr. Opin. Electrochem.* **2019**, *13*, 132-139.

10.1002/anie.202509132

Entry for the Table of Contents

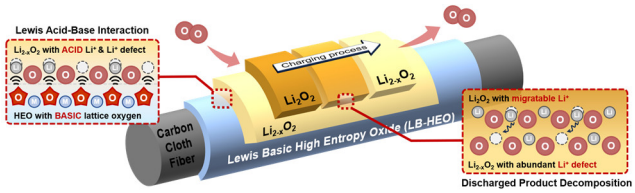

Lewis basicity of lattice oxygen is activated in our spinel-type high entropy oxide (LB-HEO). Through Lewis acid-base interaction, LB-HEO can attract acidic Li^+, leading to more disorder and Li^+ defect ($Li_{2-x}O_2$) in the discharge product (Li_2O_2) of lithium-oxygen batteries. This effectively enhances the Li^+ diffusion kinetics in Li_2O_2, which improves the interfacial electron transfer and eventually the decomposition kinetics in the charging process. It provides a new prospective of Li^+ regulation to the catalyst for lithium-oxygen batteries to achieve better electrochemical performance.